NASA TECHNICAL NOTE

NASA TN D-7494

NASA TN D-7494

REMOVAL OF SPACECRAFT-SURFACE PARTICULATE CONTAMINANTS BY SIMULATED MICROMETEOROID IMPACTS

by J. H. Goad, Jr., J. D. DiBattista, D. M. Robinson, and W. P. Chu

Langley Research Center
Hampton, Va. 23665

NATIONAL AERONAUTICS AND SPACE ADMINISTRATION • WASHINGTON, D. C. • MAY 1974

1. Report No. NASA TN D-7494	2. Government Accession No.	3. Recipient's Catalog No.
4. Title and Subtitle REMOVAL OF SPACECRAFT-SURFACE PARTICULATE CONTAMINANTS BY SIMULATED MICROMETEOROID IMPACTS		5. Report Date May 1974 6. Performing Organization Code
7. Author(s) J. H. Goad, Jr., J. D. DiBattista, D. M. Robinson, and W. P. Chu		8. Performing Organization Report No. L-9269 10. Work Unit No. 975-72-51-03
9. Performing Organization Name and Address NASA Langley Research Center Hampton, Va. 23365		11. Contract or Grant No. 13. Type of Report and Period Covered
12. Sponsoring Agency Name and Address National Aeronautics and Space Administration Washington D.C. 20546		14. Sponsoring Agency Code Technical Note

15. Supplementary Notes

W. P. Chu is a Research Associate Professor, School of Sciences, Old Dominion University, Norfolk, Va.

16. Abstract

A series of hypervelocity impacts has been conducted in an exploding lithium-wire accelerator to examine with a far-field holographic system the removal of particulate contaminants from external spacecraft surfaces subjected to micrometeoroid bombardment. The impacting projectiles used to simulate the micrometeoroids were glass spheres nominally 37 μm in diameter, having velocities between 4 and 17 km/sec. The particulates were glass spheres nominally 25, 50, and 75 μm in diameter which were placed on aluminum targets.

For these tests, particulates detached had velocities that were log-normally distributed. The significance of the log-normal behavior of the ejected-particulate velocity distribution is that the geometric mean velocity and the geometric standard deviation are the only two parameters needed to model completely the process of particles removed or ejected from a spacecraft surface by a micrometeoroid impact.

17. Key Words (Suggested by Author(s))

Contamination cloud
Micrometeoroid impacts
Particulate contaminants
Velocity distribution
Far-field holography
Particulate shedding

18. Distribution Statement

Unclassified – Unlimited

STAR Category 31

19. Security Classif. (of this report)	20. Security Classif. (of this page)	21. No. of Pages	22. Price*
Unclassified	Unclassified	30	$3.25

*For sale by the National Technical Information Service, Springfield, Virginia 22151

REMOVAL OF SPACECRAFT-SURFACE PARTICULATE CONTAMINANTS BY SIMULATED MICROMETEOROID IMPACTS

By J. H. Goad, Jr., J. D. DiBattista, D. M. Robinson, and W. P. Chu*
Langley Research Center

SUMMARY

A series of hypervelocity impacts has been conducted in an exploding lithium-wire accelerator at the Langley Research Center to examine with a far-field holographic system the removal of particulate contaminants from simulated external spacecraft surfaces subjected to micrometeoroid bombardment. The impacting projectiles used to simulate the micrometeoroids were glass spheres nominally 37 μm in diameter, having velocities between 4 and 17 km/sec. The particulates were glass spheres nominally 25, 50, and 75 μm in diameter which were placed on 127-μm-thick 6061-T6 aluminum targets. The targets were cleaned with an ethyl-alcohol-impregnated cloth before particulate emplacement and the targets were "vacuum soaked" for 1 hour at 6.6 Pa before impact.

For these tests, particulates detached from areas of 0.06, 1.00, and 10.00 cm^2 had velocities that were log-normally distributed. The significance of the log-normal behavior of the ejected-particulate velocity distribution is that the geometric mean velocity and the geometric standard deviation are the only two parameters needed to model completely the process of particles removed or ejected from a spacecraft surface by a micrometeoroid impact.

INTRODUCTION

A problem which is being increasingly recognized as critical to successful space flight is the contamination cloud which surrounds any spacecraft. This contamination cloud results from spacecraft outgassing, dumping, and dislodgement of surface materials.

---

*Research Associate Professor, School of Sciences, Old Dominion University, Norfolk, Virginia.

The cloud can be composed not only of molecular gas species but of discrete particulates as well (refs. 1 and 2). When windows and other optical elements become polluted with particulates or when optical systems must observe through the contamination cloud, the success of many experiments can be jeopardized. As an example from reference 3, particulates can scatter sunlight into a spacecraft star tracker to present a false star signal or cause a high background noise to destroy the signal from the star being tracked. Since spacecraft optical systems and optical experiments are becoming more complex and critical to mission success, data are needed to assess all the mechanisms that can remove or transport particulates in the local spacecraft environment.

One such transport mechanism that may be encountered is micrometeoroid impact. Bombardment by these small extraterrestrial hypervelocity particles can generate vibrational waves that travel out to eject particulates that are adhering to the spacecraft surface. The subsequent release of these particulates into the local spacecraft environment may then create the various problems outlined above. It is the purpose of this paper to present the particulate velocities that can be achieved through laboratory simulation of micrometeoroid impact. These velocities, when considered in the light of any body forces present between the particulates and spacecraft, have a definite bearing on whether an ejected particle leaves the vicinity of the spacecraft forever or remains in the vicinity of the spacecraft perhaps to return to another position on the spacecraft.

In this experiment the micrometeoroid bombardment was simulated by accelerating glass spheres in an exploding lithium-wire accelerator. This accelerator launches projectiles nominally 37 μm in diameter in the velocity range from 4 to 17 km/sec for impact with targets seeded with glass-bead particulates nominally 25, 50, and 75 μm in diameter. The characteristics of the particulate removal due to the impact were determined in a series of nine runs under varying experimental conditions. These included both the size and areal density of the seeding particulates as well as the energy and momentum values of the impacting projectiles. The ejected particulates were characterized as to number and velocity using a far-field holographic recording process. The energy and momentum values of the impacting projectiles were obtained from the diameter of the craters they made in the target and measurement of their in-flight velocities. The analyzed results show the statistical velocity distribution of the particulate ejection process and how it relates to such parameters as seeding size, area, and areal density and to the energy and momentum of the projectiles which impacted the targets.

SYMBOLS

d	particulate diameter, μm
K_∞	constant, 1.95×10^{-4}
m	projectile mass, g
P_∞	penetration depth or crater radius, cm
R	radial distance from impact site to the center of the seeded area, $\sqrt{x^2 + y^2}$, mm
V	velocity of impacting projectile, cm/sec
V'	velocity of ejected particulates, cm/sec
$\bar{V}$	geometric mean velocity of particulates, cm/sec
x,y	rectangular coordinates measured from center of seeded area on target, mm
λ	laser wavelength
ρ_m	projectile density, 2.7 g/cm^3
σ_g	geometric standard deviation
ϕ	log-normal probability density

TARGET CHARACTERISTICS AND PREPARATION

The targets used in the impact tests were all of 6061-T6 aluminum, 127 μm thick, 16 cm square, and clamped on the edges. Before particulate deposition, the targets were cleaned by orthogonal wipes with an ethyl-alcohol-impregnated linen cloth until no visible residue was left on the target.

The glass-bead particulates were deposited by sprinkling them on the target from a distance of approximately 10 cm. This simulates as closely and conveniently as possible the natural settling of particulates on spacecraft surfaces. The target area seeded in this manner varied according to the particulate size to reduce the time required to read up holographic and microphotographic data. For the 25-μm-diameter particulates a 0.06-cm^2 area was seeded; for the 50-μm-diameter particulates a 1.00-cm^2 area was seeded. In both these cases microphotographs were made of the total seeded area to obtain a particulate count. In the case of the 75-μm-diameter particulates, three targets were seeded – two having a 10.00-cm^2 seeded area and one having a 1.00-cm^2 seeded area. For the 75-μm-diameter case, a microphotograph and a corresponding particulate count was made of only 1.00 cm^2 of the seeded area. The seeded targets were "vacuum soaked" for 1 hour at 6.6 Pa prior to impact.

EXPLODING LITHIUM-WIRE ACCELERATOR

In order to impact particulate-seeded targets, an exploding lithium-wire accelerator was used to launch glass-bead projectiles (nominally 37 μm in diameter) in the velocity range of 4 to 17 km/sec. In the exploding lithium-wire accelerator, energy stored in a 44-kJ capacitor bank is used to vaporize a lithium wire. The projectiles to be accelerated are located on a Mylar disk located in front of the lithium wire. The vaporized lithium vaporizes the Mylar and drag accelerates the projectiles to hypervelocity. The flight distance for the projectiles between the accelerator breech and seeded target is 5.5 m. To ascertain launched projectile velocity, the accelerator is equipped with both a terminal-impact flash particle detector and an in-flight particle detector (ref. 4).

Several tests were run without the glass projectiles striking the targets to assure that lithium plasma from the explosion was not interfering with the experiments. Under these conditions, both the posttest target microphotographs and the far-field holograms revealed no particulate removal.

CALCULATION OF PROJECTILE ENERGY AND MOMENTUM

The projectile energy and momentum for each test is listed in table I. In all cases except run 6, where only one impact occurred, multiple projectile impacts occurred on the targets. Where multiple impacts occurred, the largest crater was assumed to have been made by the projectile having the highest velocity and so on down to the smallest crater which was associated with the slowest velocity. Using the following equation (see ref. 5*):

*In reference 5, V is given in km/sec and K_∞ is 0.42.

$$P_\infty = K_\infty m^{0.352} \rho_m^{1/6} V^{2/3}$$

the mass of the impacting particle is found by

$$m = \left[\frac{P_\infty}{K_\infty \rho_m^{1/6} V^{2/3}} \right]^{1/0.352}$$

With the mass determined and the projectile velocity measured, the momentum and energy can be determined. These data along with crater diameter and location are summarized in tables II, III, and IV. As a check on this procedure, the calculated projectile masses were compared to those initially loaded into the accelerator. The calculated masses listed in the tables were always in the same mass range as those loaded for launch.

As can be seen from table I, the incident energy for all cases was between 2 and 11 mJ and the incident momentum was between 7×10^{-7} and 34×10^{-7} kg-m/sec. For all the multiple-impact runs a single impact carrying the same energy can be roughly considered to have occurred on the order of 1 to 2 cm from the center of the seeded particulate area.

In run 6 where a single hypervelocity impact occurred, the impacting-particle parameters were

Density = 2.7 g/cm^3

Velocity = 11 km/sec

Mass = 1.32×10^{-7} g

Projectile diameter = 45 μm

Energy = 7.98 mJ

Momentum = 14.52×10^{-7} kg-m/sec

The radial distance from the impact site to the center of the seeded area R was 24.41 mm.

The posttest plate count and far-field holographic count of particulates given in table I are usually within a factor of 2.5 which is good considering the difficulty of the tests and the possibility of plate contamination or loss of beads during handling. However, for runs 7 and 8, the posttest target particulate count was conducted on only 1 cm^2 but the holographic count was done for particulates from several square centimeters.

EXPERIMENTAL HOLOGRAPHIC DESCRIPTION

General

Far-field or Fraunhofer holography is an ideal technique to measure the parameters of small high-speed particles (ref. 6). These parameters are size, velocity distribution, and three-dimensional location. The parameters provide information for a complete velocity analysis of particulate shedding or ejection from targets which have been impacted by simulated micrometeoroids.

In the simplest far-field holographic arrangement, a single collimated laser beam is used (see fig. 1(a)). Diffracted light waves from the object combine with the undiffracted light waves to form interference patterns which are recorded by the film plate as a hologram. The developed plate is placed into a collimated laser beam and a reconstruction of the object results at the original object-to-film-plate distance with the same object dimensions (see fig. 1(b)). Therefore, we have a technique for recording and sizing objects. Also, the original position of the object can be determined. This technique is used with small objects where the far-field condition can be satisfied (i.e., the object-to-film-plate distance must be larger than d^2/λ, where d is the object width or diameter and λ is laser wavelength). For example, if the object width or diameter is 100 μm and a red laser is used, a spacing of 2 cm or greater is required between the object and film plate.

Recording/Reconstruction Procedure

A description of the experimental procedure used to record and reconstruct the holograms of the particulate shedding can be divided into four areas: (1) the holographic recording geometry; (2) the light source and illuminating optics; (3) the synchronizing electronics; and (4) the reconstruction geometry. Each of these areas will be discussed briefly.

The recording arrangement used in this experiment to form the holograms is shown as the "holocamera" in figure 2. As can be seen this geometry differs from the simple collimated scheme outlined in figure 1. This variation is dictated primarily by the physical constraints of the test chamber. The large window-to-target distance (approximately 50 cm) necessitated the use of auxiliary optics to transfer the target area closer to the film plane. It has been shown (ref. 7) that signal-to-noise considerations in the

recorded hologram indicate that an object-to-film-plate distance of from 1 to 3 far-field distances optimizes the reconstructed image (1 far-field distance is defined as d^2/λ). Therefore the optics were chosen to image the target area to satisfy this condition. In this case an f/4, 40-cm focal length lens provided a 1:1 image and the total depth of field examined ranged approximately from 1 to 5 far-field distances.

Illumination of the particle field was provided by a Pockels cell Q-switched ruby laser. The laser output was mode controlled via an intracavity aperture (2.0 mm) and a multielement etalon. The 2.0-mm-diameter output beam was expanded to 10 cm by a diffraction-limited Galilean telescope resulting in a fully illuminated target area. The energy available for hologram exposure was limited to 20 mJ and the pulse duration was approximately 50 nsec. These laser-output parameters proved sufficient to expose the photographic plate* and to "stop" the motion of the ejected particulates.

The time interval between projectile impact and holographic exposure is used to determine the time of flight of the ejected particulates. The position of the ejected particulates from the target is determined from the reconstructed hologram. Therefore, the velocity of the particulates can be determined. Figures 2 and 3 show the complete recording system installed on the accelerator.

Reconstruction of the holograms is done using a helium-neon laser. The optical geometry, shown in figure 4, is the reverse of the recording geometry (i.e., the direction of light propagation is opposite to that used during recording). This procedure is used in order that the aberrations introduced in the recording and reconstructing steps are symmetrical (ref. 8). Enhancement of the reconstructed image is accomplished by two procedures. The first is the employment of optical filtering (ref. 9) in the Fourier transform plane of the hologram illuminating lens (see fig. 4). Results of the enhancement procedure can be seen in figure 5. This reconstruction of a typical hologram shows the ejected particles traveling from left to right. In figure 5(c), low-frequency background noise and edge-diffraction effects have been removed with a combination of high-pass and directional filters in the transform plane. The second is the use of a TV camera/monitor readout system. The brightness/contrast controls in the TV readout have provided an added flexibility in controlling the dynamic range of the holographic reconstruction (ref. 10). The combined use of these two enhancement procedures facilitates the data interpretation.

*Film speed (to obtain a density of 0.5) = 50 ergs/cm^2; Resolution = 2800 lines/mm.

HOLOGRAPHIC DATA ANALYSIS

From the holographic readout system described in the preceding sections, particulate parameters can be determined and the data analyzed. From these data, various points regarding the nature of the particulate shedding process can now be determined. For example, histograms of the ejected particulate count versus arithmetic sampling of velocity intervals did not yield a normal probability distribution (see fig. 6). The same data were plotted over equal-log sampling intervals and a skewed Gaussian profile resulted as shown in figure 7. This profile indicates that the ejected-particulate velocities are log-normally distributed (ref. 11). Also, since the particulate velocity is zero for the particulates on the target, the log-normal distribution that is zero for zero particulate velocity is the most representative and physically correct.

A more useful way to plot and examine log-normal data is to use a logarithmic probability graph. The percent of all particulates with a velocity less than the stated velocity is plotted versus the logarithm of the stated velocity. This is shown for run number 8 in figure 8. True log-normal distributions represent a straight line on a logarithmic probability graph as explained by Aitchison and Brown in reference 12. To verify a mathematical model of log-normality, curve fitting techniques defined in references 12 and 13 can be used to compare experimental data to the log-normal probability-density equation. However, a logarithmic probability graph is accepted as indicating statistical significance as discussed in references 11 and 12. When the data plotted on a logarithmic probability graph is a straight line, the geometric mean velocity $\overline{V}$ and geometric standard deviation σ_g can be easily obtained. The geometric mean velocity $\overline{V}$ is the velocity at the 50 percent point on the plot. In reference 11 the geometric standard deviation σ_g is given by

$$\sigma_g = \frac{84.13\% \text{ velocity}}{50\% \text{ velocity}} = \frac{50\% \text{ velocity}}{15.87\% \text{ velocity}}$$

The form of the log-normal probability-density equation is (refs. 11 and 12)

$$\phi = \frac{1}{\log_e \sigma_g \sqrt{2\pi}} \exp\left[-\frac{(\log_e V' - \log_e \overline{V})^2}{2 \log_e{}^2 \sigma_g}\right]$$

The geometric standard deviation σ_g is related to the slope of the straight line on the logarithmic probability graph. Also, it is a measure of the skewness (ref. 12) of the log-normal probability-density equation when plotted over an arithmetic graph. Since all experimental data points have some scatter, techniques must be used to obtain the best straight line fit on the logarithmic probability graph. As in reference 14, the points closest to the 50 cumulative percent should be heavily weighted as this is the peak of the Gaussian profile when plotted on an equal-log interval graph. Also, most investigators, as cited by Smith and Jordan in reference 11, attach strong significance only to the experimental points between 20 to 80 cumulative percent.

Figures 9, 10, and 11 are plots of the measured particulate velocities where the data points are fitted by straight lines on a logarithmic probability graph. From these, the geometric mean velocity $\overline{V}$ and the geometric standard deviation σ_g were determined for all runs and listed in table I. The minimum geometric mean velocity was 3.2 cm/sec and the maximum was 13.5 cm/sec. This velocity spread was small but the variation in the energy and momentum of the impacting projectiles was also small (see table I). From the experimental data, the lowest velocity recorded was 0.52 cm/sec and the highest velocity was 152 cm/sec.

From table I, it can be seen that the magnitude of the geometric mean velocity $\overline{V}$ relates to the energy and momentum of the impacting projectile. In general, the larger energy and momentum impacts produce higher geometric mean velocities of the ejected particulates. In addition, for the three different diameters of the seeding particulates, the magnitude of the geometric mean velocities of the ejected particulates and the geometric standard deviations were independent of the size and areal density of the seeding particulates.

Figures 9, 10, and 11 would appear to indicate that the velocity distributions are bimodal below the 20 to 30 cumulative percentage points. In this lower velocity region, the target edge diffraction combines with the particulate diffraction to produce high noise in the holographic recording. In figure 5, this can be seen close to the target surface. Because of this noise effect, a single particulate not counted in this region of the plot is a significant portion of the cumulative percent. Therefore, the bimodality can arise from the experimental technique.

The significance of the log-normal behavior of the ejected-particulate velocity distribution is that the geometric mean velocity and the geometric standard deviation are the

only two parameters needed to model completely the process of particles removed or ejected from a spacecraft surface by a micrometeoroid impact.

CONCLUSIONS

A series of hypervelocity impacts has been conducted in an exploding lithium-wire accelerator at the Langley Research Center to examine with a far-field holographic system the removal of particulate contaminants from simulated external spacecraft surfaces subjected to micrometeoroid bombardment. The impacting projectiles used to simulate the micrometeoroids were glass spheres nominally 37 μm in diameter, having velocities between 4 and 17 km/sec. The particulates were glass spheres nominally 25, 50, and 75 μm in diameter which were placed on 127-μm-thick 6061-T6 aluminum targets.

Under the experimental conditions described in this paper, several conclusions regarding the nature of the particulate removal or shedding process from micrometeoroid-impacted spacecraft-type structures can be reached. First, the particulates that were ejected from the targets had velocities that were log-normally distributed. The significance of the log-normal behavior of the ejected-particulate velocity distribution is that the geometric mean velocity $\overline{V}$ and the geometric standard deviation σ_g are the only two variables needed to model completely the process of particles removed or ejected from a spacecraft surface by a micrometeoroid impact. Second, the variables of the log-normal distribution (i. e., $\overline{V}$ and σ_g) were independent of particulate size, areal density, and seeded area for the size range tested. Finally, it may generally be stated the larger the energy and momentum of the impacting projectiles the higher the geometric mean velocities of the ejected particulate.

Langley Research Center,
National Aeronautics and Space Administration,
Hampton, Va., February 4, 1974.

REFERENCES

1. Naumann, R. J.: Design Principles for Contamination Abatement in Scientific Satellites. Paper presented at the XXIII International Astronautical Congress, Design Aspects of Scientific Satellites II (Vienna, Austria), Oct. 10, 1972.

2. Paul, F. W.: Degradation Due to Contaminants Throughout the Test Cycle. Optical Telescope Technology, NASA SP-233, 1970, pp. 751-757.

3. Anon.: Spacecraft Star Trackers. NASA Space Vehicle Design Criteria (Guidance and Control). NASA SP-8026, 1970, pp. 23-27.

4. Robinson, D. M.; Chu, W. P.; and Goad, J. H.: In-Flight Detection of Small Hypervelocity Particles. Appl. Opt., vol. 12, no. 7, July 1973, pp. 1524-1529.

5. Anon.: Meteoroid Damage Assessment. NASA Space Vehicle Design Criteria (Structures). NASA SP-8042, 1970, pp. 29-30.

6. DeVelis, J. B.; and Reynolds, George O.: Theory and Applications of Holography. Addison-Wesley Pub. Co., c.1967, p. 40.

7. Reynolds, G. O.; and DeVelis, J. B.: Hologram Coherence Effects. IEEE Trans. Antennas & Propagation, vol. AP-15, no. 1, Jan. 1967, pp. 41-48.

8. Smith, Warren J.: Modern Optical Engineering. McGraw-Hill Book Co., Inc., c.1966, p. 333.

9. Goodman, Joseph W.: Introduction to Fourier Optics. McGraw-Hill Book Co., Inc., c.1968, p. 141.

10. Robinson, Don M.: Interim Tests on a Holographic Technique for Photographing High-Speed Mil-Size Particles. Holographic Instrumentation Applications, NASA SP-248, 1970, pp. 221-235.

11. Smith, John Elvans; and Jordan, Myra Lee: Mathematical and Graphical Interpretation of the Log-Normal Law for Particle Size Distribution Analysis. J. Colloid Sci., vol. 19, 1964, pp. 549-559.

12. Aitchison, J.; and Brown, J. A. C.: The Lognormal Distribution. Cambridge Univ. Press, 1957.

13. Kottler, F.: The Goodness of Fit and the Distribution of Particle Sizes. J. Franklin Inst., vol. 251, no. 5, May 1951, pp. 499-642.

14. Kottler, F.: The Distribution of Particle Sizes. J. Franklin Inst., vol. 250, no. 4, Oct. 1950, pp. 339-441.

TABLE I.- PROJECTILE AND PARTICULATE PARAMETERS

Run number	Particulate nominal diameter, μm	Impacting projectiles		Beads removed		Geometric mean velocity, $\overline{V}$, cm/sec	Geometric standard deviation, σ_g
		Kinetic energy, mJ	Momentum, kg-m/sec	Posttest target count	Far-field holographic count		
1	25	2.07	8.8×10^{-7}	63	67	3.2	3.2
2	25	4.68	9.5	43	28	3.6	2.6
3	25	10.48	33.3	107	44	13.5	2.4
4	50	5.06	18.93×10^{-7}	90	88	8.5	2.6
5	50	5.99	13.23	113	120	10.6	3.0
6	50	7.98	14.52	26	42	7.4	2.2
*7	75	3.04	10.50×10^{-7}	15	38	3.4	2.3
*8	75	9.55	22.99	53	226	7.3	2.1
9	75	2.38	7.89	28	31	5.3	1.8

*Posttest bead count from target area of 1 cm^2.

TABLE II.- TARGET AND PROJECTILE PARAMETERS FOR TESTS USING PARTICULATES OF A NOMINAL DIAMETER OF 25 μm

Crater diameter, $2P_\infty$, cm	Projectile velocity, V, km/sec	Coordinates of crater		$R = \sqrt{x^2 + y^2}$, mm	Calculated values for projectile		
		x, mm	y, mm		Mass, g	Momentum, kg-m/sec	Energy, mJ
Run number 1							
0.00904	5.5	13.5	-18.0	22.5	0.63×10^{-7}	3.5×10^{-7}	0.95
.00762	4.9	-3.0	15.0	15.3	.48	2.3	.58
.00534	3.7	22.0	-2.0	22.1	.28	1.0	.19
.00534	3.6	-8.5	-7.5	11.3	.30	1.1	.19
.00428	3.5	10.0	5.0	11.2	.18	.6	.11
.00334	3.2	13.5	-.5	13.5	.10	.3	.05
				Total	1.97×10^{-7}	8.8×10^{-7}	2.07
Run number 2							
0.01048	10.4	-1.5	-7.0	7.1	0.29×10^{-7}	3.0×10^{-7}	1.57
.01048	10.0	-10.0	3.0	10.4	.31	3.1	1.55
.00952	9.1	7.5	5.0	9.0	.28	2.5	1.16
.00666	9.0	-1.0	9.0	9.0	.10	.9	.40
				Total	0.98×10^{-7}	9.5×10^{-7}	4.68
Run number 3							
0.01382	7.7	-11.0	-6.0	12.5	1.12×10^{-7}	8.6×10^{-7}	3.32
.01283	7.4	2.5	8.0	8.4	.98	7.2	2.68
.00858	5.5	-11.0	8.5	13.9	.55	3.0	.83
.00810	5.5	-11.0	3.0	11.4	.46	2.5	.69
.00762	5.0	-2.0	16.5	16.6	.47	2.3	.59
.00714	5.0	11.0	-5.0	12.1	.39	1.9	.49
.00714	5.0	-11.0	5.5	12.3	.39	1.9	.49
.00714	5.0	-1.0	.5	1.1	.39	1.9	.49
.00618	4.7	5.0	-8.5	9.8	.29	1.4	.32
.00618	4.7	14.0	9.0	16.0	.29	1.4	.32
.00428	4.2	6.0	-13.0	14.3	.13	.5	.11
.00428	4.2	-12.0	11.5	16.6	.13	.5	.11
.00286	3.5	1.0	-13.5	13.5	.06	.2	.04
				Total	5.65×10^{-7}	33.3×10^{-7}	10.48

TABLE III.- TARGET AND PROJECTILE PARAMETERS FOR TESTS USING PARTICULATES OF A NOMINAL DIAMETER OF 50 μm

Crater diameter, $2P_\infty$, cm	Projectile velocity, V, km/sec	Coordinates of crater		$R = \sqrt{x^2 + y^2}$, mm	Calculated values for projectile		
		x, mm	y, mm		Mass, g	Momentum, kg-m/sec	Energy, mJ
Run number 4							
0.01096	6.0	0	12.0	12.0	0.93×10^{-7}	5.58×10^{-7}	1.67
.00810	5.6	2.0	-10.0	10.2	.45	2.52	.70
.00810	5.6	.5	3.0	3.04	.45	2.52	.70
.00714	5.5	-2.5	11.0	11.28	.32	1.76	.48
.00714	5.3	-5.0	17.0	17.72	.35	1.85	.49
.00666	5.1	10.5	9.0	13.83	.31	1.58	.40
.00524	4.4	7.0	18.5	19.78	.20	.88	.19
.00418	4.2	18.0	0	18.00	.13	.55	.11
.00418	4.2	11.5	6.5	13.21	.13	.55	.11
.00382	4.0	11.0	14.0	17.84	.10	.40	.08
.00334	3.8	2.5	-5.0	5.59	.08	.30	.06
.00334	3.4	12.0	14.0	18.44	.09	.31	.05
.00238	3.2	-3.0	-9.0	9.48	.04	.13	.02
				Total	3.58×10^{-7}	18.93×10^{-7}	5.06
Run number 5							
0.01096	17.0	-5.0	19.0	19.65	0.13×10^{-7}	2.21×10^{-7}	1.88
.00810	10.0	-7.5	-8.5	11.33	.15	1.50	.75
.00762	8.1	-.5	6.0	6.02	.19	1.54	.62
.00714	7.2	2.0	-11.5	11.67	.19	1.37	.49
.00714	7.2	-5.0	3.0	5.83	.19	1.37	.49
.00714	7.2	-2.5	3.5	4.30	.19	1.37	.49
.00666	6.7	-5.0	3.5	6.10	.18	1.21	.40
.00618	6.6	-11.0	-11.0	15.55	.15	.99	.33
.00618	6.6	-8.5	11.5	14.30	.15	.99	.33
.00524	6.2	-5.0	-1.5	5.22	.11	.68	.21
				Total	1.63×10^{-7}	13.23×10^{-7}	5.99
Run number 6							
0.01856	11.0	20.0	14.0	24.41	1.32×10^{-7}	14.52×10^{-7}	7.98

TABLE IV.- TARGET AND PROJECTILE PARAMETERS FOR TESTS USING PARTICULATES OF A NOMINAL DIAMETER OF 75 μm

Crater diameter, $2P_\infty$, cm	Projectile velocity, V, km/sec	Coordinates of crater		$R = \sqrt{x^2 + y^2}$, mm	Calculated values for projectile		
		x, mm	y, mm		Mass, g	Momentum, kg-m/sec	Energy, mJ
Run number 7							
0.01096	7.3	-12.5	-9.0	15.40	0.65×10^{-7}	4.74×10^{-7}	1.73
.00810	6.8	-22.5	-14.0	26.50	.31	2.11	.72
.00524	3.4	-18.0	-8.0	19.69	.33	1.12	.19
.00524	3.4	-26.0	-1.0	26.02	.33	1.12	.19
.00476	3.0	-10.0	-7.0	12.21	.31	.93	.14
.00334	3.0	-11.0	-1.5	11.10	.11	.33	.05
.00238	3.0	-10.0	-3.0	10.44	.05	.15	.02
				Total	2.09×10^{-7}	10.50×10^{-7}	3.04
Run number 8							
0.01286	10.3	-17.0	-1.5	17.06	0.53×10^{-7}	5.46×10^{-7}	2.81
.01286	8.8	-5.0	-1.0	5.10	.71	6.25	2.75
.00952	7.8	-20.0	1.5	20.0	.38	2.96	1.15
.00764	7.8	26.0	13.0	29.0	.20	1.56	.61
.00762	7.8	-24.0	-9.5	25.8	.20	1.56	.61
.00714	7.5	-16.0	-13.5	20.9	.18	1.35	.51
.00618	6.6	-15.5	-10.5	18.72	.15	.99	.33
.00572	6.1	-14.5	0	14.50	.14	.85	.26
.00572	5.0	-9.5	-15.5	18.18	.21	1.05	.26
.00524	4.9	-5.5	-.3	5.50	.17	.83	.20
.00286	4.5	-1.5	-1.0	1.8	.03	.13	.06
				Total	2.90×10^{-7}	22.99×10^{-7}	9.55
Run number 9							
0.01094	6.4	9.0	14.0	16.64	0.82×10^{-7}	5.25×10^{-7}	1.68
.00666	5.5	15.0	6.0	16.15	.27	1.48	.41
.00382	5.4	25.0	7.0	25.96	.06	.32	.09
.00334	4.8	22.0	5.0	22.56	.05	.24	.06
.00334	4.4	13.0	12.0	17.69	.06	.26	.06
.00286	4.3	23.0	7.5	24.19	.04	.17	.04
.00286	4.3	4.0	9.5	10.30	.04	.17	.04
				Total	1.34×10^{-7}	7.89×10^{-7}	2.38

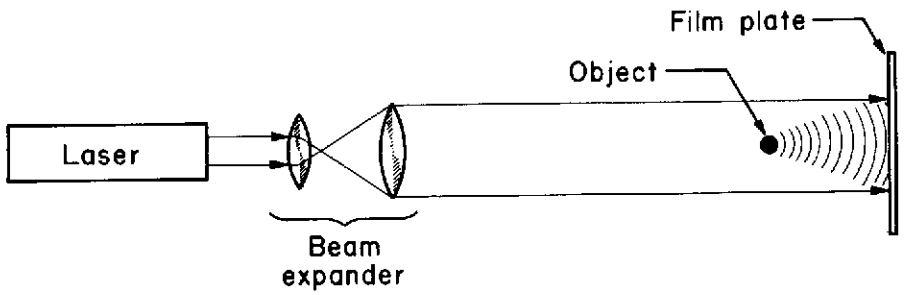

(a) Construction.

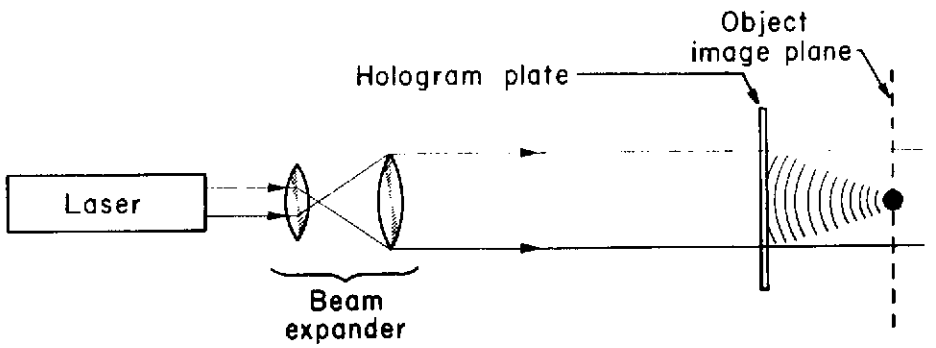

(b) Reconstruction.

Figure 1.- Typical construction and reconstruction of a far-field hologram.

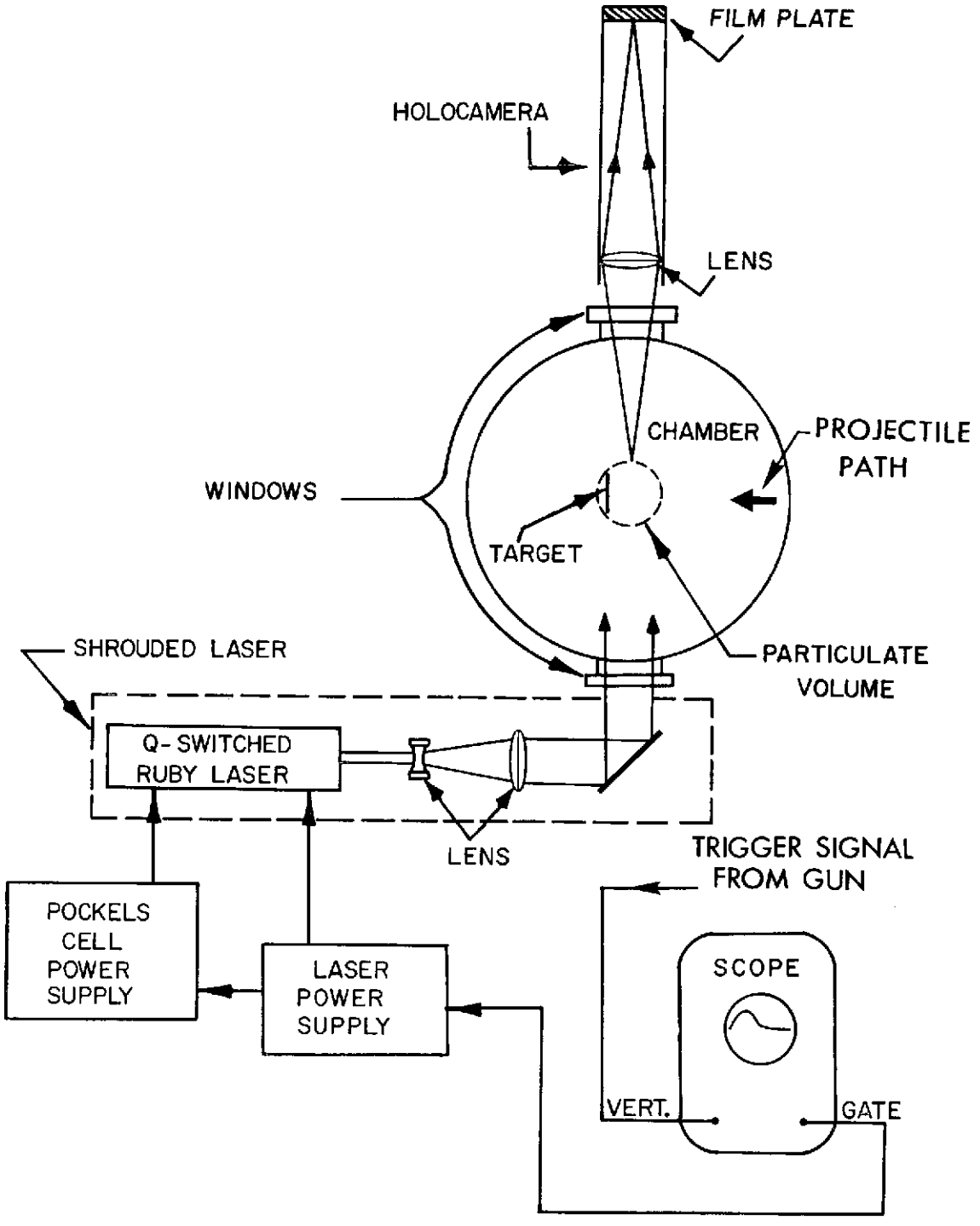

Figure 2.- Block diagram of the far-field holographic system installed on the target chamber of the exploding lithium-wire accelerator.

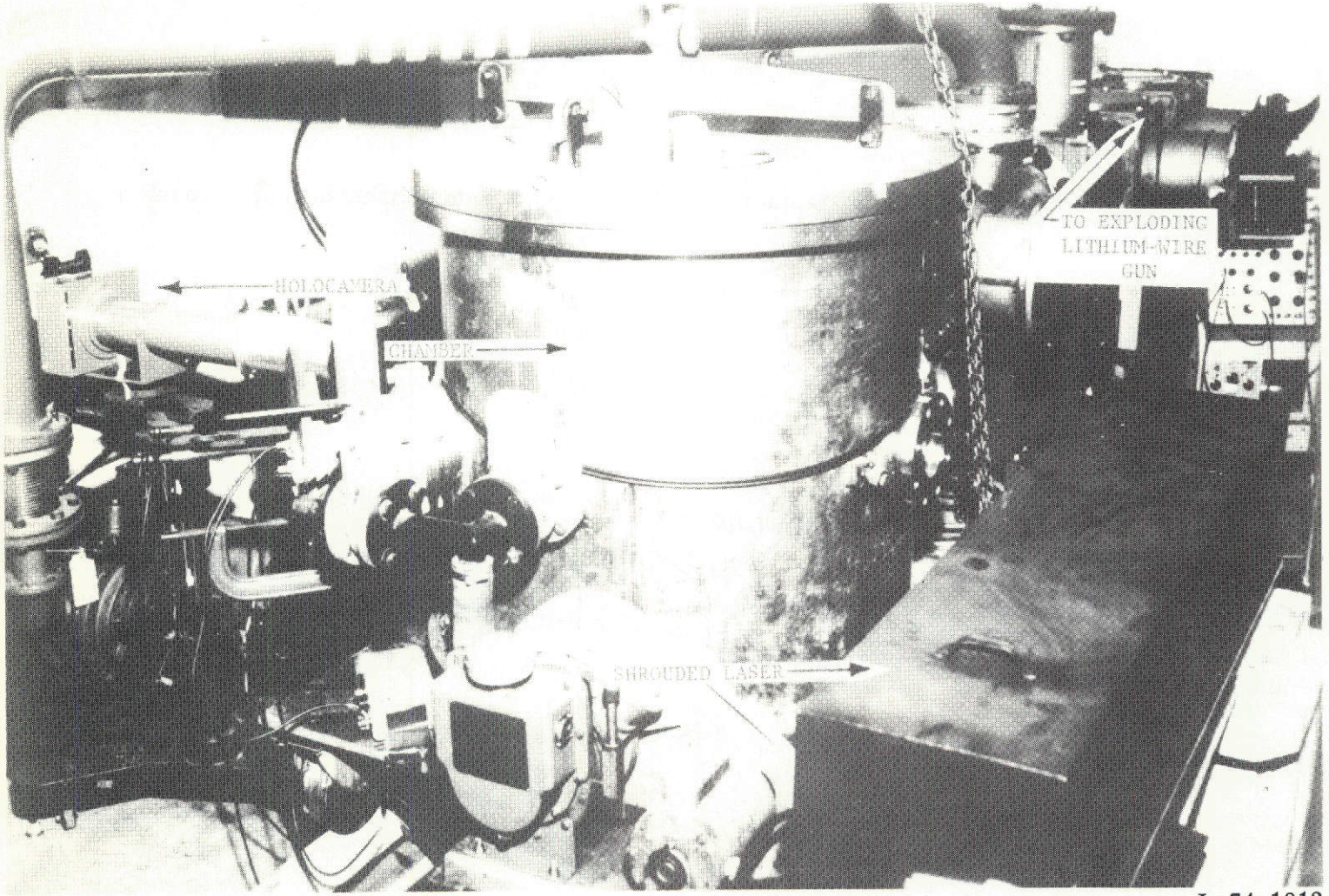

L-74-1012

Figure 3.- Holographic system and exploding lithium-wire gun.

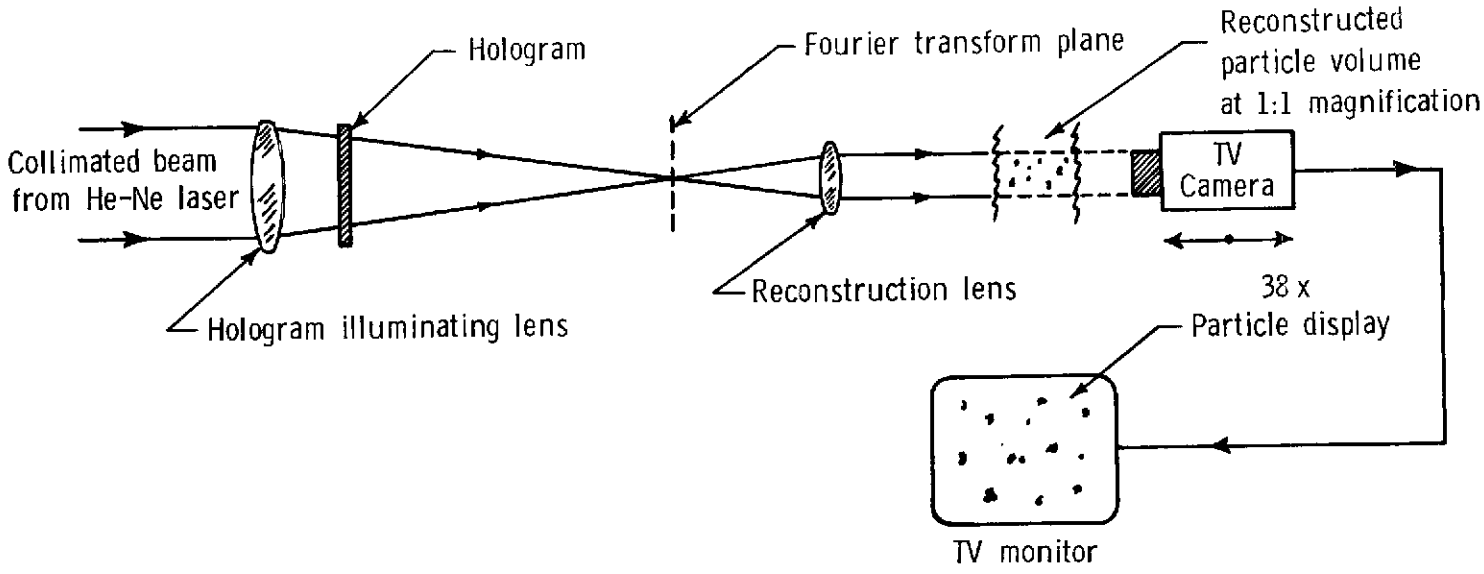

Figure 4.- Reconstruction optics. Geometry is symmetrical to recording geometry.

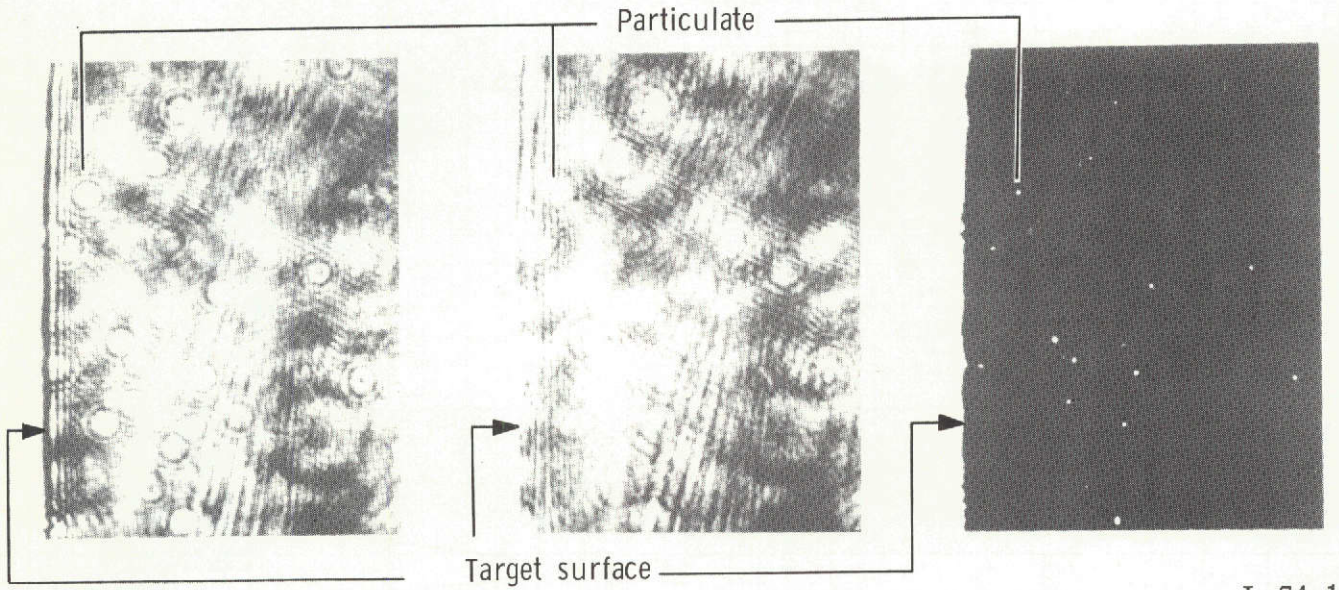

(a) Hologram. (b) Reconstruction. (c) Enhanced reconstruction.

Figure 5.- Typical hologram of particulates of a nominal diameter of 75 μm ejected from target by impacting projectiles. (Height of photographed section is 1 cm.)

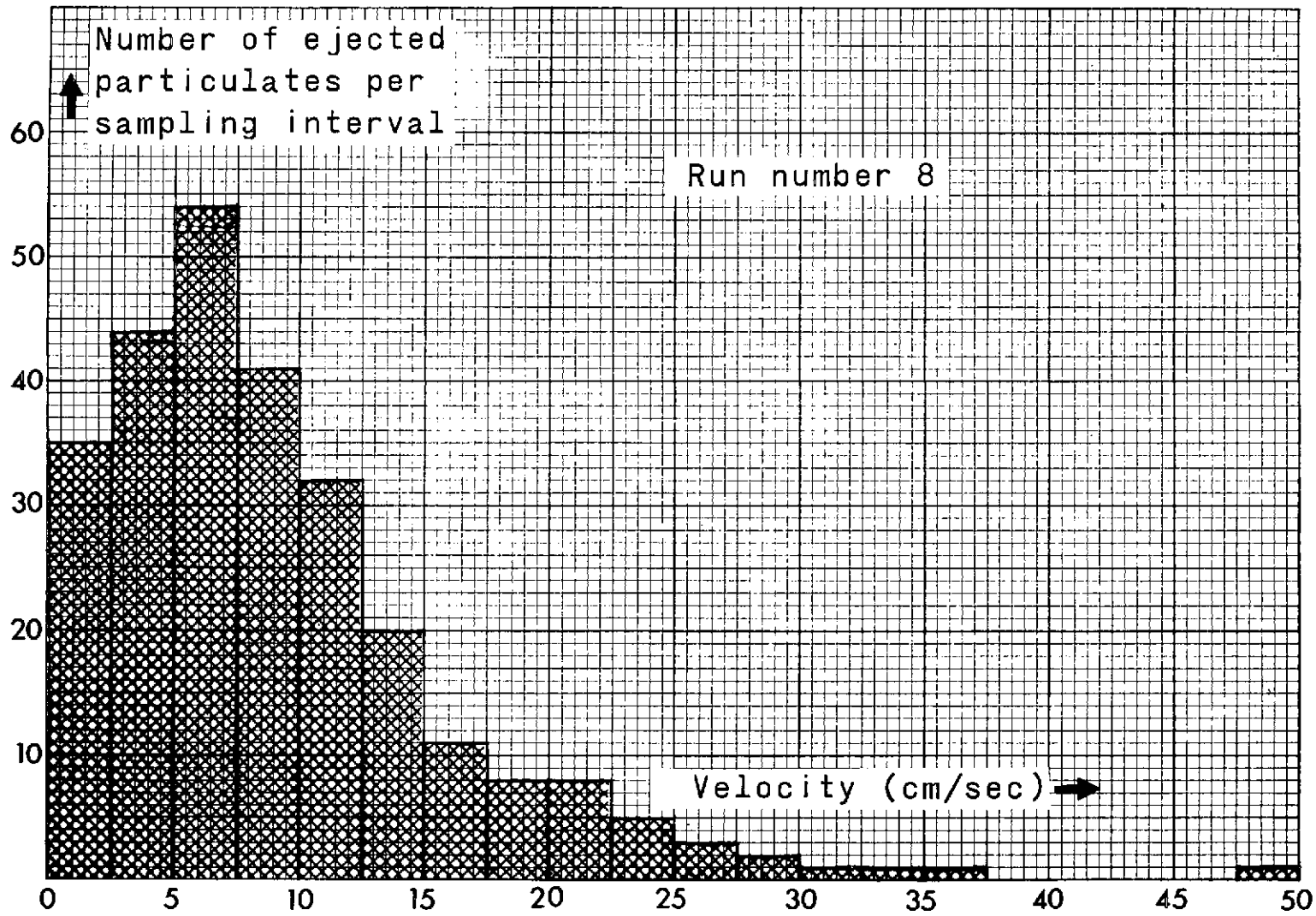

Figure 6.- Histogram: Number of particulates ejected from target per arithmetic velocity interval.

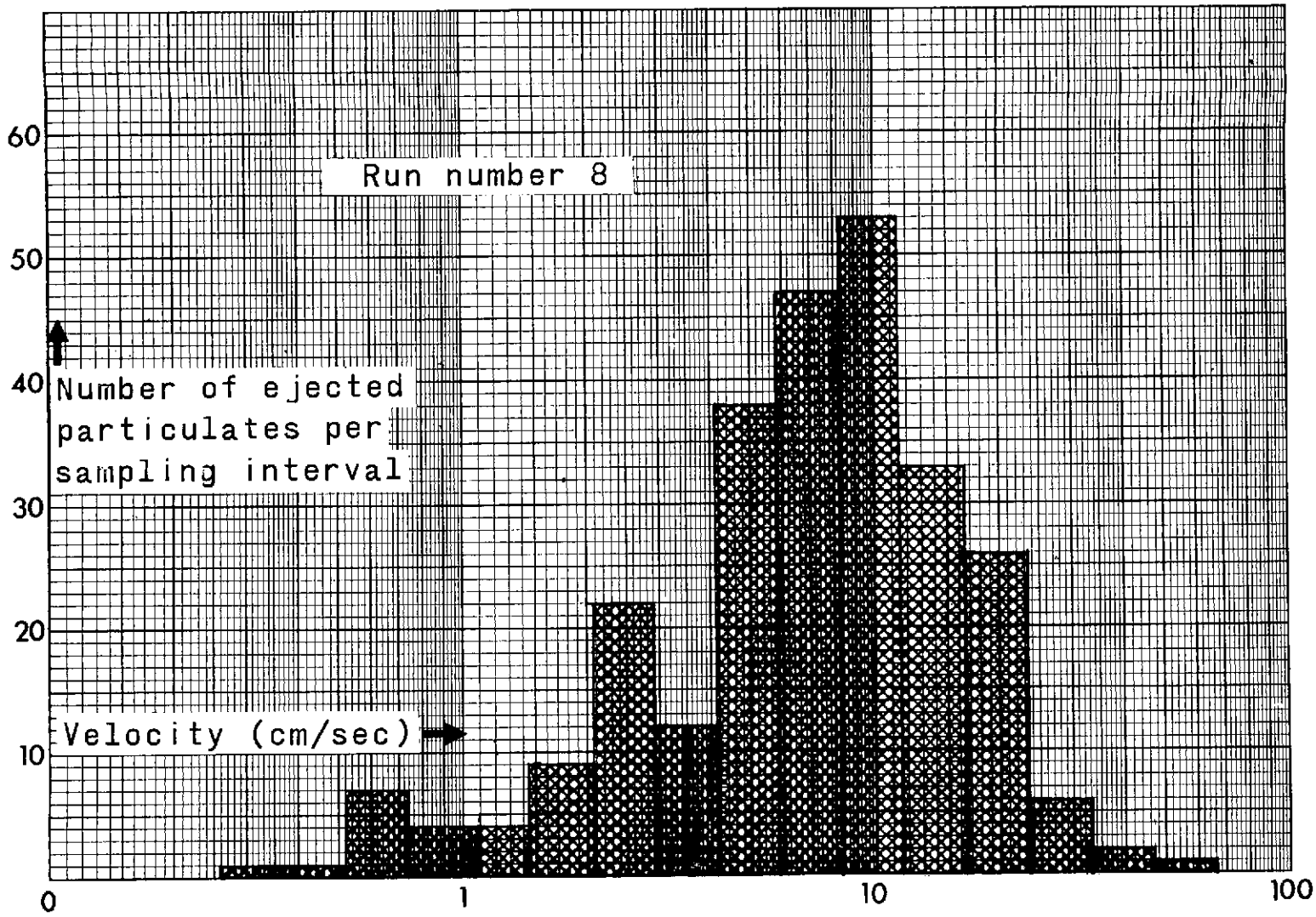

Figure 7.- Histogram: Number of particulates ejected from target per equal-log velocity interval.

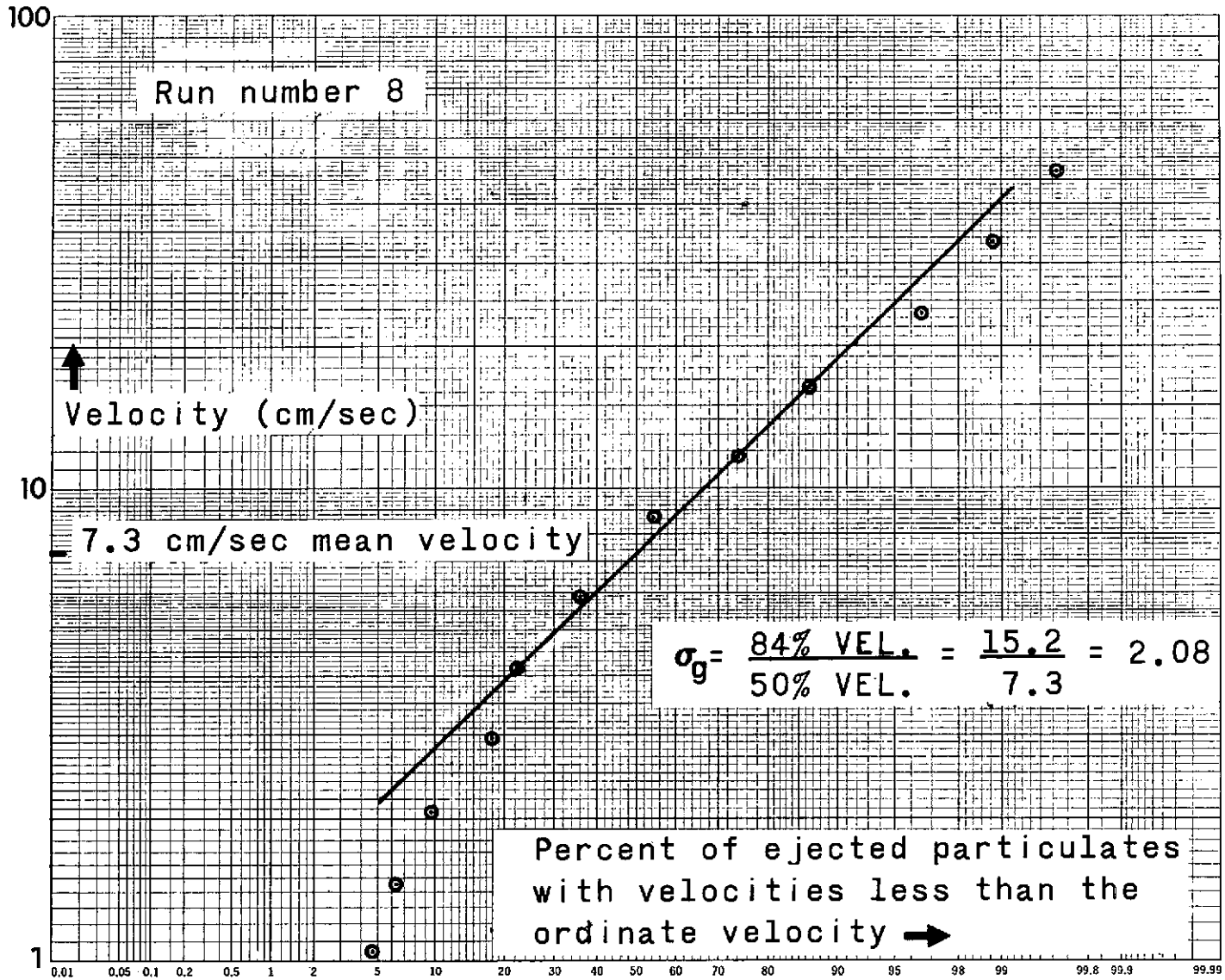

Figure 8.- Logarithmic probability graph of particulates ejected from target.

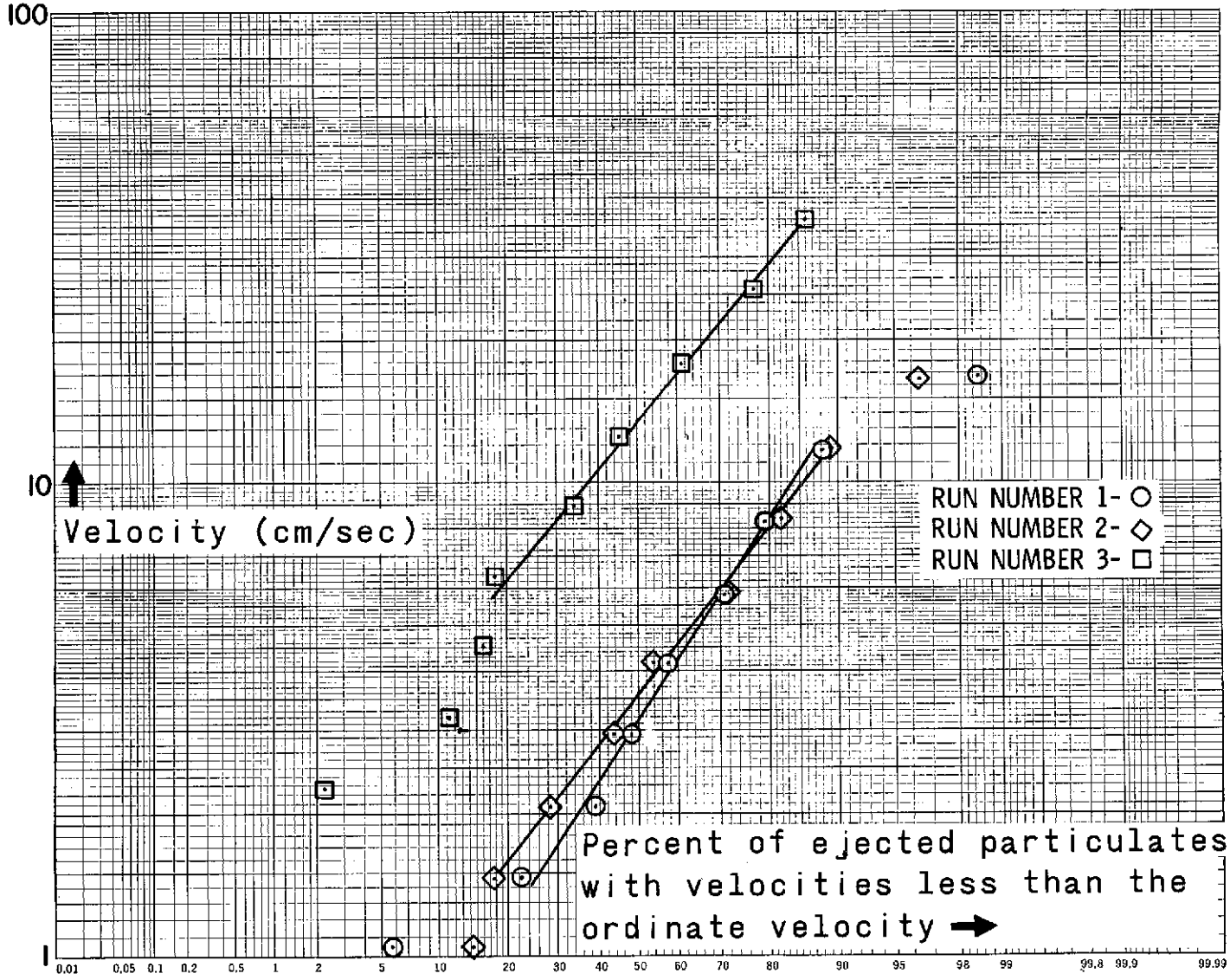

Figure 9.- Logarithmic probability graph of particulates of a nominal diameter of 25 μm ejected from target.

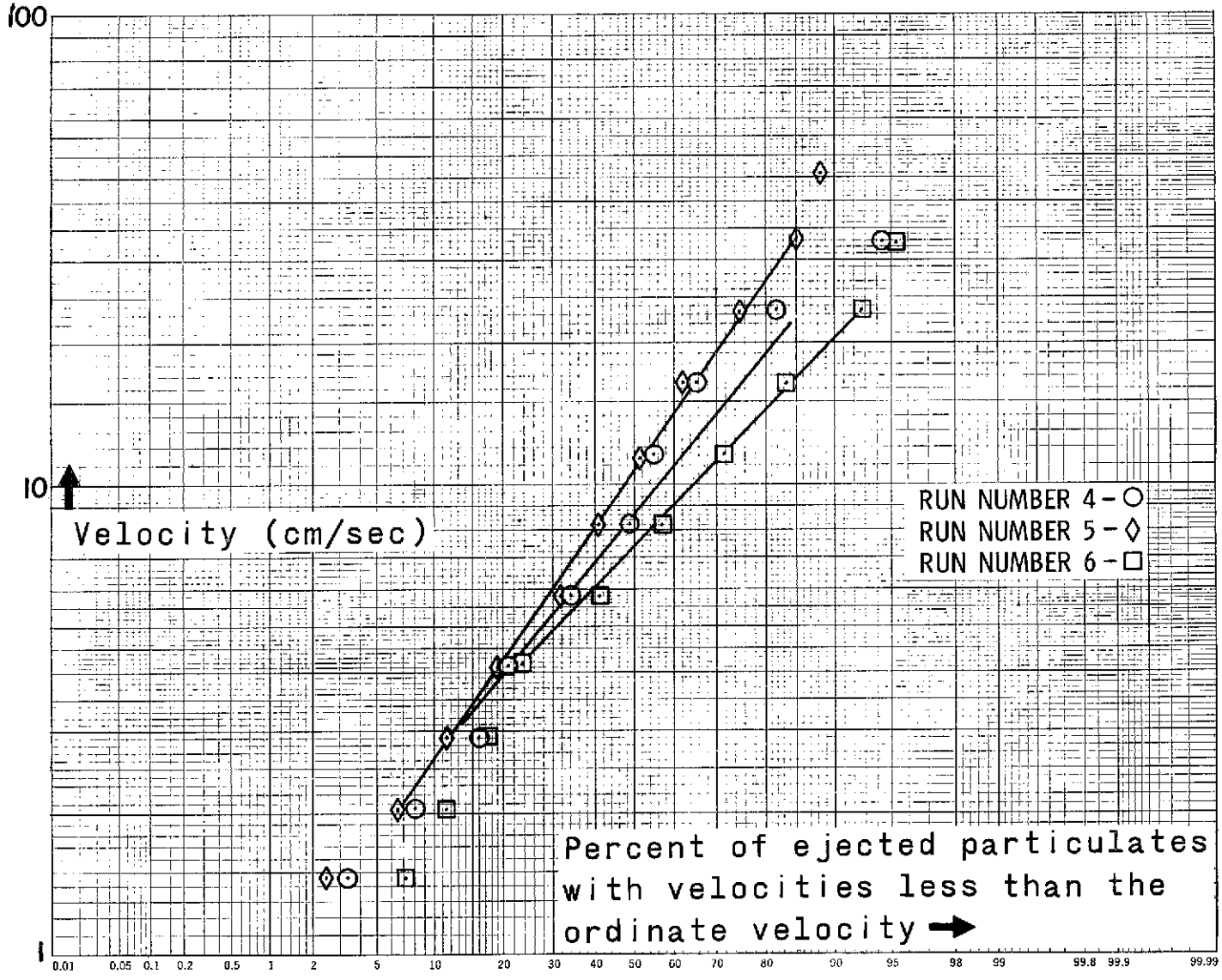

Figure 10.- Logarithmic probability graph of particulates of a nominal diameter of 50 μm ejected from target

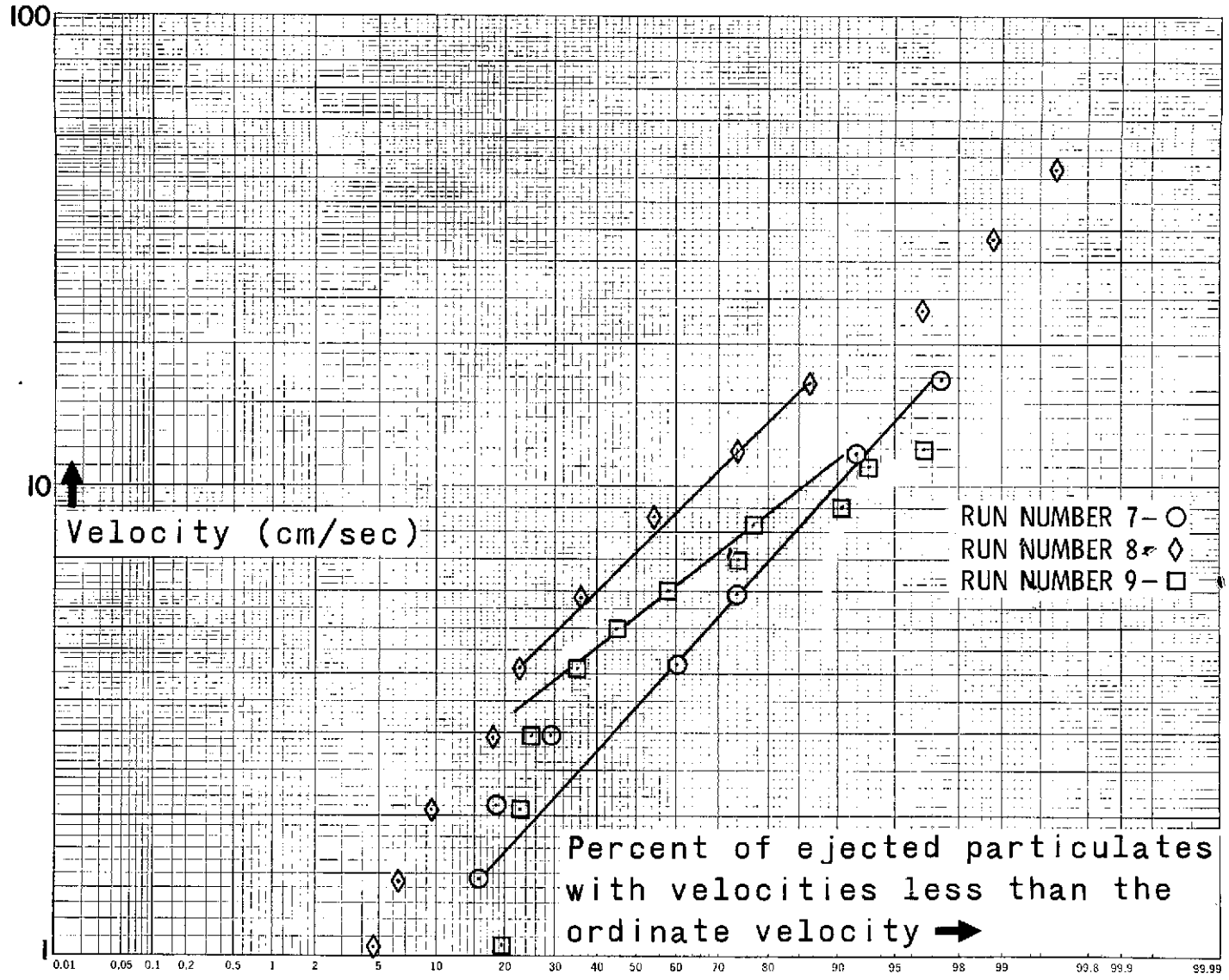

Figure 11.- Logarithmic probability graph of particulates of a nominal diameter of 75 μm ejected from target.